Received: 23 July 2024 | Revised: 20 January 2025 | Accepted: 18 February 2025

DOI: 10.1002/mrm.30490

RESEARCH ARTICLE

Magnetic Resonance in Medicine

A steady-state MR fingerprinting sequence optimization framework applied to the fast 3D quantification of fat fraction and water T1 in the thigh muscles

Constantin Slioussarenko | **Pierre-Yves Baudin** | **Benjamin Marty**

Neuromuscular Investigation Center, NMR Laboratory, Institute of Myology, Paris Cedex 13, France

Correspondence
Constantin Slioussarenko, Institute of Myology, Neuromuscular Investigation Center, NMR Laboratory, G.H. Pitié-Salpêtrière–Bâtiment Babinski, 47/83 boulevard de l'Hôpital, 75651 Paris Cedex 13, France.
Email: c.slioussarenko@institut-myologie.org

Funding information
Agence Nationale de la Recherche, Grant/Award Number: ANR-20-CE19-0004

Abstract

Purpose: The aim of this study was to develop an optimization framework to shorten GRE-based MRF sequences while keeping similar parameter estimation quality.

Methods: An optimization framework taking into account steady-state initial longitudinal magnetization, undersampling artifacts, and mitigating overfitting by drawing from a realistic numerical thighs phantom database was developed and validated on numerical simulations and 10 healthy volunteers.

Results: The sequences optimized with the proposed framework decreased the original sequence duration by 30% (8 s per repetition instead of 11.2 s) while showing improved accuracy (SSIM going up from 96% to 99% for *FF*, from 93% to 96% for $T1_{H2O}$ on numerical simulations) and precision, especially when compared with sequences optimized through other means.

Conclusions: The proposed framework paves the way for fast 3D quantification of *FF* and $T1_{H2O}$ in the skeletal muscle.

KEYWORDS

MR fingerprinting, sequence optimization, skeletal muscle

1 | INTRODUCTION

Over the past decade, Magnetic Resonance Fingerprinting (MRF) has emerged as a prominent method for the fast and concurrent measure of multiple MRI parameters.[1] Initially proposed for measuring T1 and T2 relaxation times in neuroimaging applications, MRF has since been extended to other body regions such as the heart,[2] liver,[3] and skeletal muscles.[4] In these organs, MRF can simultaneously measure parameters such as fat fraction (FF), water T1 ($T1_{H2O}$), water T2 ($T2_{H2O}$), and fat T1 ($T1_{fat}$), which show potential as valuable imaging biomarkers.[5] In skeletal muscle, the MRF T1-FF sequence has recently been developed to simultaneously estimate FF and water T1, serving as proxies for disease severity and active muscle damage, respectively.[5] When used in conjunction with a Gadolinium-based contrast agent, the sequence also enables the estimation of extracellular volume, which has demonstrated high-sensitivity in detecting subtle alterations in muscle tissue under dystrophic conditions.[6]

The principle of MRF relies on acquiring a series of undersampled images using variable sequence parameters, and subsequent pixel-wise fitting to a pre-computed dictionary of signal evolutions for estimating the tissue parameters. A key advantage of MRF is thus the flexibility in designing the acquisition schedule. Early implementations often used either pseudo-random or physics-driven schemes to vary sequence parameters such as TE, TR, RF flip angles (FA), and phases. However, optimizing the sequence to enhance sensitivity to specific tissue parameters is often desirable, leading to the rapid development of theoretical frameworks aimed at sequence optimization and shorter scan time. Initial optimization frameworks assumed that MRF acquisition noise was Gaussian, focusing on minimizing the correlation between dictionary signals[7,8] or the Cramer-Rao lower bound.[9] However, it has been shown that errors in MRF parameter maps are primarily driven by the undersampling artifacts in the image series, which cannot be modeled as independent Gaussian variables. Consequently, recent MRF optimization frameworks aim to either simulate these artifacts[10,11] or predict them using analytical formulas.[12,13] These frameworks were initially designed for MRF sequences estimating two parameters, specifically T1 and T2, and applied on numerical brain phantoms to optimize the MRF sequences. For instance, Jordan et al. simulated undersampling errors by clustering the brain numerical phantom into four distinct regions (each corresponding to different pairs of T1 and T2 parameters) and pre-computing the undersampling errors on the corresponding cluster masks to accelerate the optimization process.[10] This approach, however, would result in a prohibitive number of clusters for sequences estimating more parameters simultaneously, such as the MRF T1-FF sequence, which aims to estimate five parameters ($T1_{H2O}$, $T1_{Fat}$, FF, off-resonance frequency (df) and B1) for skeletal muscle applications.[4] Heestersbeek et al. derived an analytical formula to predict the error caused by undersampling and optimized the flip angle train by minimizing it using Sequential Least Square Programming,[13] which might lead to a local optimum for the solution.[14] Furthermore, these frameworks did not consider the potential overfitting problem caused by using a numerical phantom with a single shape and parameter distribution during the iterative optimization process.

Several MRF sequences use trains of fast gradient echo (GRE) readouts with varying parameters. These sequences offer multiple options for handling the residual transverse magnetization: either balanced,[15] unbalanced[16] or spoiled gradient echo using the Fast Low Angle Shot (FLASH) method.[17] For example, FLASH MRF sequences use RF-spoiling in addition to gradient spoiling to mitigate transverse magnetization before the next RF pulse is applied. This approach is effective for estimating B1 from the fingerprints while remaining insensitive to T2, with a relatively simple signal evolution model for the dictionary generation, which is the case for the recently developed MRF T1-FF sequence.[4] Another sequence, Plug-and-Play MRF uses radial sampling with two FLASH segments for B1 and T1 encoding and two Fast Imaging with Steady-state Precession (FISP) segments for T2 encoding, enabling T1, T2, and B1 estimation in the liver.[18] A downside of GRE-based MRF sequences is their generally long recovery times between repetitions, necessary for the longitudinal magnetization to return to equilibrium, significantly increasing the overall acquisition time when the repetition of the MRF scheme is mandatory. This extended period becomes particularly problematic in multi-shot spiral MRF acquisitions[19] or 3D MRF imaging.[20] Reducing the recovery time following the fast GRE train would be highly beneficial in these applications. Previous empirical studies have explored steady-state MRF sequences with reduced recovery time to shorten scan duration.[20]

In this work, we propose a framework for optimizing the TE and FA schedules, and recovery time of GRE-based MRF sequences, applied to the quantification of $T1_{H2O}$, FF, as well as df, B1, and $T1_{Fat}$ in the skeletal muscles. This framework uses an analytical formula to calculate the steady-state of the initial magnetization of each repetition of the MRF scheme. It also simulates undersampling artifacts using realistic numerical thigh phantoms and mitigates potential overfitting by varying the shape and parameter distribution of the phantom through the iterations of the optimization process.

2 | METHODS

The reference sequence for this work was the MRF T1-FF sequence, which consists of an initial inversion followed by a train of 1400 readouts acquired with golden angle radial sampling. This sequence uses a FLASH readout with varying TE and FA, and enables the reconstruction of a time-series of 175 undersampled images with different contrasts.[4] A 3D version of this sequence was proposed by acquiring partitions sequentially and using golden angle radial stack-of-stars sampling.[21] In these initial implementations, each repetition of the MRF scheme included a four-second recovery time to allow the magnetization to return to equilibrium. Reducing this recovery time results in a steady-state for the longitudinal magnetization at the beginning of each repetition of the MRF scheme, as demonstrated in the following section.

2.1 | Steady-state initial longitudinal magnetization analytical formula

In the most generic case, for a GRE train of N RF pulses of flip angles $(\theta_i)_{i=1,\dots,N}$, echo time $(TE_i)_{i=1,\dots,N}$ and repetition time $(TR_i)_{i=1,\dots,N}$, we have:

$$\begin{aligned} &M_x(t_- + TE_i) = [M_x(t_-)cos(\phi_i) - \\ &(M_y(t_-)cos(\theta_i) - M_z(t_-)sin(\theta_i))sin(\phi_i))]E_{2,i} \\ &M_y(t_- + TE_i) = [M_x(t_-)sin(\phi_i) + \\ &(M_y(t_-)cos(\theta_i) - M_z(t_-)sin(\theta_i))cos(\phi_i))]E_{2,i} \\ &M_z(t_- + TR_i) = M_0 + \\ &(M_y(t_-)sin(\theta_i) + M_z(t_-)cos(\theta_i) - M_0)E_{1,i} \end{aligned} \tag{1}$$

where t_- denotes time right before excitation, the phases $(\phi_i)_{i=1,\dots,N}$ include off-resonance and gradient dephasing effects, $E_{1,i} = e^{-\frac{TR_i}{T_1}}$ and $E_{2,i} = e^{-\frac{TE_i}{T_2}}$.

For ease of notation, TR_N includes as well the recovery time before the next repetition of the sequence.

Assuming perfect transverse magnetization spoiling in the case of a FLASH GRE train, these equations can be rewritten as:

$$M_x(t_- + TE_i) = M_z(t_-)sin(\theta_i)sin(\phi_i)E_{2,i} \tag{2}$$

$$M_y(t_- + TE_i) = -M_z(t_-)sin(\theta_i)cos(\phi_i)E_{2,i} \tag{3}$$

$$M_z(t_- + TR_i) = M_0 + (M_z(t_-)cos(\theta_i) - M_0)E_{1,i} \tag{4}$$

We observe that the transverse magnetization depends only on $M_z(t_-)$. Therefore, to demonstrate the existence of a steady-state, it is sufficient to show that Equation (4) produces a steady-state after a few repetitions.

To simplify the notations, let's assume $M_0 = 1$ and define: $u_i = M_z(t_- + TR_i)$, $a_i = E_{1,i}\cos(\theta_i)$ and $b_i = 1 - E_{1,i}$. Additionally, we define $v_p = u_{p(N+1)}$, with v_p denoting the initial magnetization after p repetitions of the entire MRF scheme. Our objective is to show that v_p reaches a steady-state. We have:

$$u_i = a_{i-1}u_{i-1} + b_{i-1} \tag{5}$$

By recursion, we can show that:

$$v_p = Av_{p-1} + B \tag{6}$$

where we define $A = \prod_{i=0}^{N} a_i$ and $B = \sum_{i=0}^{N}(\prod_{j=N-i+1}^{N} a_j)\, b_{N-i}$. Since $|A| < 1$, it follows that a steady state M_z^{SS} is reached, given by:

$$M_z^{SS} = \frac{B}{1 - A} \tag{7}$$

The formula above was derived for a single component. For a mixture and fat and water, the steady-state is given by the mixture of the steady states for each component with their respective T1 and T2.

2.2 | Sequence Optimization Framework

The proposed MRF optimization framework consists of 5 blocks as illustrated in Figure 1: (1) Dictionary simulation for steady-state MRF FLASH sequences with initial inversion and variable TE and FA; (2) Simulation of undersampled image series of realistic numerical thigh phantoms; (3) MRF pattern matching; (4) Cost function evaluation; and (5) Minimization algorithm.

The target variables for optimization were the acquisition parameters $(\theta_i)_{i=1,\dots,N}$, $(TE_i)_{i=1,\dots,N}$ and recovery time TR_N. The repetition times $(TR_i)_{i=1,\dots,N-1}$ were set to the minimum value allowed by the gradient system and the TEs. To reduce the problem's dimensionality, we fixed the TE schedule to have a piecewise constant evolution with three steps and parametrized the FA evolution using a smooth function of nine parameters, eight parameters $\rho_j, \psi_j, j = 1, \dots, 4$ for controlling the overall shape of the curve, and the 9th parameter α for rescaling the curve between 5° and α:

$$\begin{aligned} \hat{\theta}_i &= \sum_{j=1}^{4} \rho_j * \sin(2j\pi i/N + \psi_j) \\ \theta_i &= \frac{\hat{\theta}_i - \min_i(\hat{\theta}_i)}{\max_i(\hat{\theta}_i) - \min_i(\hat{\theta}_i)} * (\alpha - 5°) + 5° \end{aligned} \tag{8}$$

This left us with a total of 16 parameters to optimize: The number of readouts N, three TE values and two-step timings, nine FA parameters and the recovery time TR_N. N was constrained to lie between 520 and 1 400 (the number of spokes in MRF T1-FF). TE values were bounded between 2 ms (close to the minimum TE allowed by the sequence RF pulses and gradient system) and 6 ms. As mentioned above, FA was constrained to be greater than 5° ensuring a sufficient signal-to-noise ratio.

For each iteration of the optimization algorithm, the acquisition parameters were used to simulate a bi-component MRF dictionary using extended phase graph (EPG) simulations (https://github.com/py-baudin/epgpy), starting from the steady-state magnetization value (as determined by Equation (7)). The dictionary was simulated for the following grid of tissue and experimental parameters: $T1_{H2O}$ from 600 ms to 1 000 ms by stepsize of 100 ms, then from 1 000 ms to 1 500 ms by stepsize of 100 ms, and finally from 1 500 ms to 2 000 ms by stepsize of 100

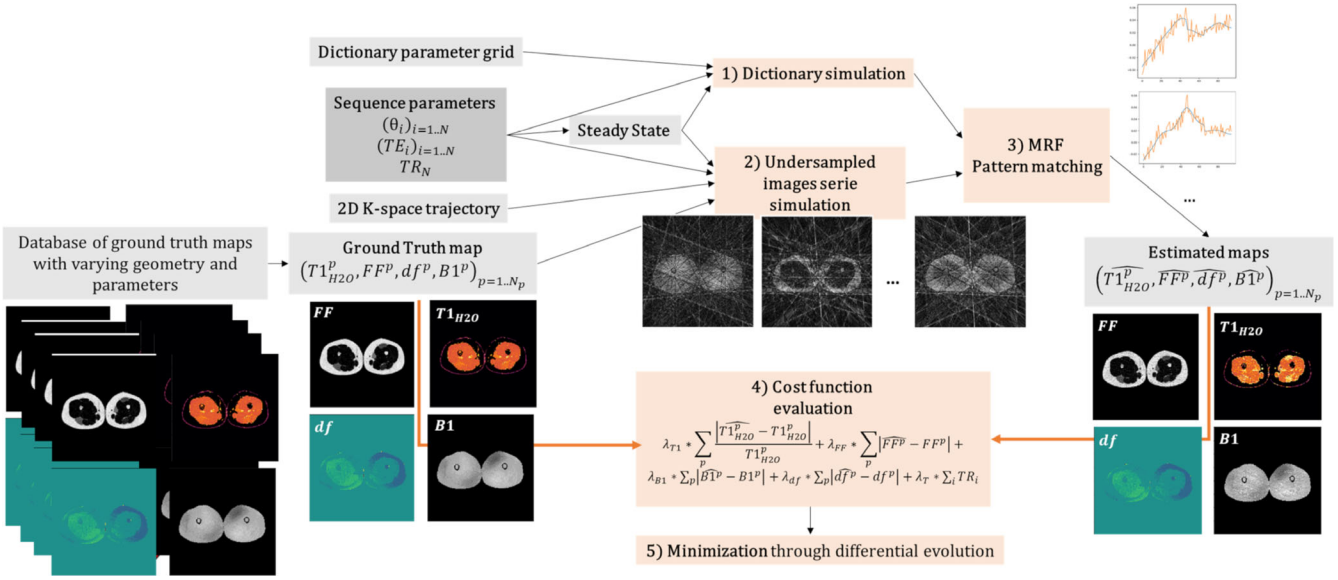

FIGURE 1 Diagram illustrating the different blocks in the proposed MRF optimization framework. The inputs to the main blocks are shown in gray: Dictionary parameter grid, current sequence acquisition parameters, and ground-truth numerical thigh phantoms database. The numerical thigh phantoms vary in geometry and parameters across the iterations of the minimization to mitigate potential overfitting. The main blocks of the optimization framework are: (1) Dictionary simulation block for steady-state MRF Flash sequences with initial inversion and variable TE and FA; (2) Undersampled images series simulation block generating the undersampled images from realistic numerical thigh phantoms; (3) MRF pattern matching block; (4) Cost function evaluation block; and (5) Minimization block.

ms; $T1_{Fat}$ fixed to 300 (ms); $df \in [-90, -60, -45, -30, -15, 0, 15, 30, 45, 60, 90]$ (Hz); B1 from 0.5 to 1.5 by stepsize of 0.1. $T2_{H2O}$ and $T2_{Fat}$ were fixed respectively to 40 ms and 80 ms. The short readouts and combined RF and gradient spoiling make the sequences insensitive to T2.[21]

We also simulated the undersampled time-series obtained by the current MRF sequence on realistic numerical thigh phantoms. The numerical phantoms used as ground truth were constructed from the parametric maps for each parameter obtained from an in vivo MRF T1-FF acquisition on a healthy control. To mitigate overfitting to a specific shape, a database of numerical phantoms was used, allowing random alternation between 10 different slices of the thigh acquisition at each iteration. Parameter overfitting was further mitigated by varying FF and $T1_{H2O}$ in arbitrarily chosen muscles of the thigh. The ground truth magnetization evolution simulated from the parametric maps using EPG was used to generate the k-space data for each N readout using golden-angle radial sampling, as prescribed in MRF T1-FF, and transformed to image space using non-uniform Fourier transform (nuFFT).[22,23] The images were reconstructed by using groups of 8 readouts, as for MRF T1-FF described in,[4] leading to 40× undersampling.

Pixelwise pattern matching was then performed between the time-series of images and the generated dictionary using bi-component matching to obtain the estimated parametric maps.[24]

The cost function C of the optimization framework was defined as the error between the estimated maps and the ground-truth maps, with a penalty on sequence duration:

$$\begin{aligned} &C(N, (\theta_i)_{i=1,\dots,N}, (TE_i)_{i=1,\dots,N}, TR_N) = \\ &\lambda_{T1} \sum_p \frac{|\widehat{T1^p_{H2O}} - T1^p_{H2O}|}{T1^p_{H2O}} + \\ &\lambda_{FF} \sum_p |\widehat{FF^p} - FF^p| + \\ &\lambda_{B1} \sum_p |\widehat{B1^p} - B1^p| + \\ &\lambda_{df} \sum_p |\widehat{df^p} - df^p| + \\ &\lambda_T \sum_{i=1,\dots,N} TR_i \end{aligned} \tag{9}$$

Here $T1^p_{H2O}$, FF^p, $B1^p$, df^p (resp. $\widehat{T1^p_{H2O}}$, $\widehat{FF^p}$, $\widehat{B1^p}$, $\widehat{df^p}$) denote the ground truth (resp. estimated) parameters for every pixel p in the numerical phantom mask. The penalty weighting factors were empirically set to ensure a balanced distribution between the cost function terms, overweighting $T1_{H2O}$ which we found to be more complicated to estimate especially when shortening sequence duration: $\lambda_{T1} = 2$, $\lambda_{FF} = 2$, $\lambda_{B1} = 1$, $\lambda_{df} = 0.004$, $\lambda_T = 0.01$, with df in Hz in the cost function.

The optimization algorithm used for minimizing the cost function was differential evolution.[25] Differential evolution was chosen as the optimization algorithm due to its effectiveness in handling problems where calculating the gradient of the cost function is not straightforward and for finding the global minimum of functions. The algorithm works by assessing the cost function of an initial population, then progressively refining candidates by selecting the best solutions and generating new ones through random combinations of elements, ensuring a comprehensive exploration of the solution space. The Python implementation from the SciPy library (https://scipy.org) was utilized, with default settings for both the recombination rate and mutation constant. The total number of iterations was set to 100, but the algorithm converged in fewer steps. The optimal number of spokes under the described optimization framework converged to 1 024, which was then used as a reference for all other optimized sequences.

We compared the accuracy and precision of the different MRF-derived parameters both on numerical phantoms and in vivo between the original MRF T1-FF and five other sequences: (i) the MRF T1-FF shortened to 1 024 spokes (MRF T1-FF 1 024), (ii) a sequence of 1 024 spokes minimizing the correlation between dictionary signals[7] (MRF-Cohen), (iii) a sequence of 1 024 spokes minimizing Cramer-Rao Lower Bound[9] (MRF-CRLB), (iv) a sequence using the proposed framework without varying numerical phantom parameters during the optimization process (MRF-Optim1), and (v) a sequence with varying *FF* and $T1_{H20}$ randomly across iterations as described above (MRF-Optim2). All methods used differential evolution as a minimization algorithm.

2.3 | Numerical Phantoms Simulations

The six MRF sequences were evaluated using two sets of numerical phantom data derived from quantitative $T1_{H2O}$, *FF*, *B*1, *df* and $T1_{fat}$ maps acquired in vivo from healthy volunteers with the original MRF T1-FF sequence. Dataset 1 was generated from the thigh numerical phantoms used in the optimization framework while Dataset 2 was generated from acquisitions on a different subject to check for potential overfitting to the specific geometry of the numerical phantom during optimization. For each dataset, 50 numerical phantoms were created by randomly bumping *FF* between 0 and 0.5 and $T1_{H2O}$ between 0 and 200 ms across arbitrarily chosen muscles. The matrix size of the numerical thigh phantoms was 200×200. For each MRF sequence and each numerical phantom, the undersampled image series were simulated using EPG and nuFFT, and the estimated maps were produced using bi-component dictionary fitting.[24]

2.4 | In vivo MR acquisitions

All MRI experiments were conducted on a 3T clinical MRI system (*Magnetom Prisma*^{Fit}, Siemens Healthineers, Erlangen, Germany). The protocol was approved by the local ethics committee (Comité de Protection des Personnes (CPP) Ile de France VI), and written informed consent was obtained from all volunteers. The six MRF sequences were acquired in the thighs of 10 healthy volunteers (6 men, 4 women, mean age 38.5 ± 13.6 years). The subjects were positioned head-first and supine. The body coil was used for RF transmission, and signals were acquired using a 32-channel spine receive coil combined with an 18-channel flexible surface coil placed on the volunteer's thighs. All MRF acquisitions used a radial stack of stars sampling,[26] similarly to 3D MRF T1-FF. The acquisitions were performed in the axial orientation with the following sequence parameters: Readout bandwidth = 540 Hz/px, field of view = $40 \times 40 \times 12$ cm^3 and spatial resolution = $2 \times 2 \times 5$ mm^3. An acquisition with a 1 mm in-plane resolution, which is standard in clinical neuromuscular studies,[27,28] was also performed on the thighs of a healthy volunteer to assess the generalizability of the optimized sequences to higher spatial resolutions. The six-peak lipid model, previously established at 3T in an earlier study[29] and discussed in prior MRF T1-FF research,[4,21] was used for processing the in vivo MRF acquisitions.

2.5 | Data analysis and validation metrics

From the bi-component dictionaries computed for each version of the MRF sequence, we evaluated the correlation between dictionary elements.

For both numerical phantom simulations and in vivo acquisitions, thirteen individual muscles of the thighs were automatically delineated using an open-source segmentation algorithm (https://github.com/fabianbalsiger/minimal-annotation-muscle-segmentation). The regions of interest (ROI) included the *vastus lateralis* (VL), *vastus intermedius* (VI), *vastus medialis* (VM), *rectus femoris* (RF), *sartorius* (SAR), *gracilis* (GRA), *semimembranosus* (SM), *semitendinosus* (ST), *biceps femoris* long head (BF), *biceps femoris* short head (BF-SH), *adductor magnus* (AM), and *adductor longus* (AL) muscles (Figure 2).

For the numerical phantoms, the distribution of ROI-level differences between the estimated and ground truth MRF parameters was calculated for all MRF sequences in both datasets to assess accuracy and precision. The similarity of the maps to the ground truth was visually assessed and quantified using the structured similarity index (SSIM).[30] For in vivo acquisitions, the quality

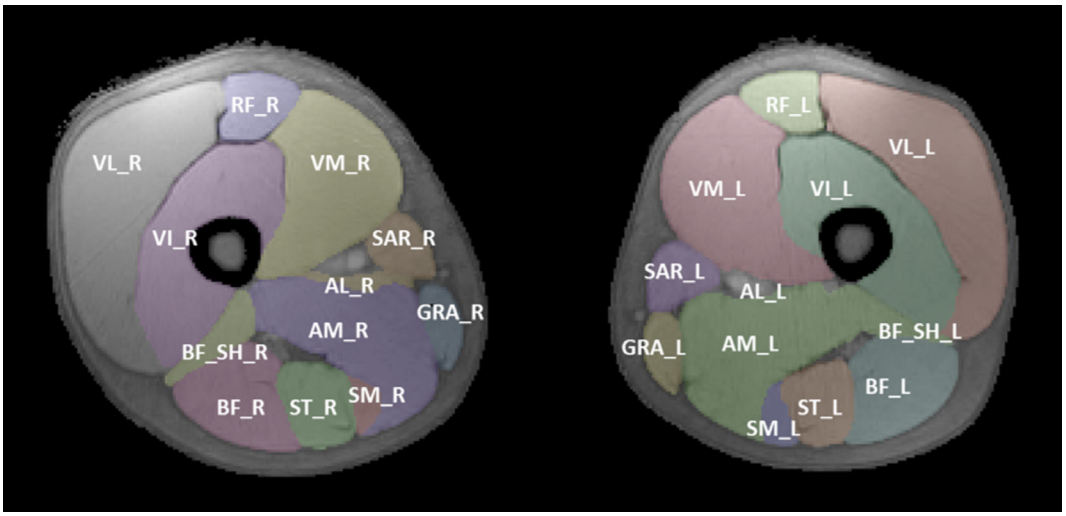

FIGURE 2 ROIs drawn from the automated segmentation illustrated in one example slice of an in vivo acquisition of both thighs: VL–*vastus lateralis*; VI–*vastus intermedius*; VM–*vastus medialis*; RF–*rectus femoris*; SAR–*sartorius*; GRA–*gracilis*; SM–*semimembranosus*; ST–*semitendinosus*; BF–*biceps femoris*; BF_SH–*biceps femoris* Short Head; AM–*adductor magnus*; AL–*adductor longus*. The L and R suffixes are used to denote the left or right thigh. The ROIs were used for random parameter bumping during optimization (MRF-Optim2), for building the numerical phantom datasets (Datasets 1 and 2), and for calculating ROI-level metrics.

of the parametric maps was visually assessed for all subjects. To evaluate the precision obtained by the different MRF sequences on FF and $T1_{H2O}$, the standard deviation for each ROI averaged across all subjects was calculated, along with the associated 95% confidence interval. The same metrics were also calculated for the other parameters estimated with the sequences (df, B1, and $T1_{Fat}$).

Statistical tests were performed to quantify the significance of the results. A one-sided T-test adjusted with Bonferroni correction was conducted to test the null hypothesis that the mean of SSIM for each optimized MRF sequence was less than MRF T1-FF. The significance of the standard deviation difference across all ROIs was tested using an ANOVA test with Bonferroni correction for multiple testing.

3 | RESULTS

3.1 | Comparison of acquisition schedules and dictionary signals

The TE and FA schedules of the five shorter MRF sequences compared in this study are shown in Figure 3, along with a selected fingerprint corresponding to the following parameters: $T1_{H2O} = 1\,400$ ms, $FF = 0.2$, $df = 90$ Hz, $B1 = 1$, $T1_{Fat} = 300$ ms. The TE schedules of MRF-Optim1 and MRF-Optim2 sequences closely resemble that of the original MRF T1-FF sequence, with only slight variation in timing and values. However, their FA schedules feature a single peak bell-shaped curve. In contrast, the TE schedules for MRF-CRLB and MRF-Cohen differ significantly in both TE values and step timings. MRF-CRLB alternates between two TE values, while its FA schedule has two peaks. Notably, the maximum FA during the readout train is significantly higher for MRF-Cohen (around 45°) compared to the other sequences (around 20°). The sample fingerprint shows the sharpest variations around the TE steps for MRF-Optim1 and MRF-Optim2 sequences. MRF-Cohen, on the other hand, exhibits minimal variation across the fingerprint, except right after the initial inversion. The recovery times TR_N were 2.75 s for MRF T1-FF 1 024, 2.80 s for MRF-Optim1, 3.00 s for MRF-Optim2, 3.00 s for MRF-CRLB and 2.65 s for MRF-Cohen. Consequently, MRF T1-FF had an acquisition time of 11.40 s per repetition, MRF T1-FF 1 024 8.10 s, MRF-Optim1 8.10 s, MRF-Optim2 8.10 s, MRF-CRLB 10.10 s and MRF-Cohen 8.90 s. Hence, for in vivo 3D acquisitions of 24 partitions, the scan time was around 4 min 40 s for MRF T1-FF, around 3 min 15 s for MRF T1-FF 1 024, MRF-Optim1 and MRF-Optim2, around 4 min for MRF-CRLB and over 3 min 30 s for MRF-Cohen.

The correlations between dictionary signals and a selected example signal were calculated and provided in Supplementary Figures S1 and S2. MRF-Cohen displayed the steepest decline in correlation when tissue parameters deviated from the reference signal, consistent with its optimization for minimizing the correlation between dictionary elements. MRF-Optim1 and MRF-Optim2 showed only a moderate decorrelation of signals along the FF and $T1_{H2O}$ directions.

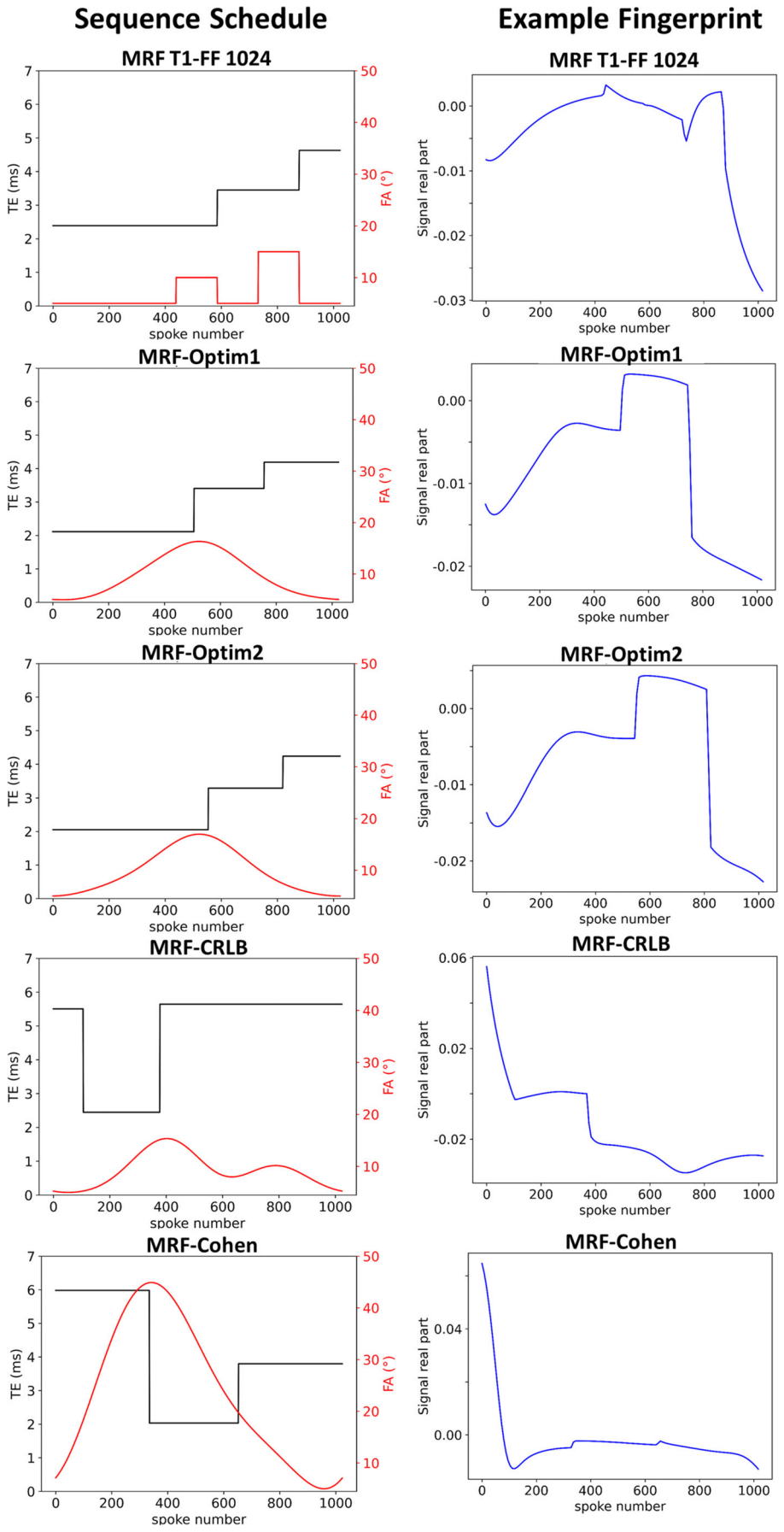

FIGURE 3 Sequence parameter schedules and sample fingerprint for all sequences. The sample fingerprint corresponds to the following tissue parameters: $T1_{H20} = 1\,400$ ms, $FF = 0.2$, $df = 90$ Hz, $B1 = 1$, and $T1_{Fat} = 300$ ms.

3.2 | Validation on Numerical Phantoms

For the numerical phantoms, $T1_{H20}$ and *FF* maps for one sample from Dataset 1 and one sample from Dataset 2 are shown in Figure 4, with corresponding *df* and B1 maps shown in Figure S3. These samples were chosen because of their distinct geometry and parameter distribution. MRF-Cohen, which minimizes correlation between dictionary signals, shows a large overestimation of $T1_{H20}$ in certain regions and exhibits pronounced streaking artifacts overall. The *FF* maps appear almost binary, with many pixel values clustering at 0 or 1, which is particularly noticeable in the subcutaneous fat. MRF-CRLB parametric maps also display a high-level of noise for both *FF* and $T1_{H2O}$, along with prominent streaking artifacts for $T1_{H20}$. Compared to the original sequence, MRF T1-FF 1 024 amplifies streaking artifacts, as expected due to its shorter duration. In contrast, MRF-Optim1 and MRF-Optim2 sequences reduce streaking artifacts in both parametric maps, even when compared to the original version of MRF T1-FF. This improvement is especially noticeable in the SAR, GRA, SM, and VL muscles, and in areas with increased $T1_{H2O}$ and *FF*. These visual assessments were confirmed by SSIM values, with MRF-Optim1 and MRF-Optim2 maps consistently showing the highest values for these two examples. The B1 maps seemed to retain most of the streaking artifacts for all sequences.

The SSIM against the ground truth maps was calculated for both datasets for all MRF sequence versions, and the overall distributions across all numerical phantoms are shown in Figure 5. For Dataset 1, MRF T1-FF 1024 shows a slight median reduction in SSIM. However, both MRF-Optim1 and MRF-Optim2 demonstrate improvement compared with MRF T1-FF, with SSIM increasing from 94.5% to over 99% for *FF* and from 93% to over 94% for $T1_{H2O}$). In dataset 2, the improvement in SSIM with MRF-Optim1 and MRF-Optim2 compared to MRF T1-FF was less pronounced, with SSIM increasing from 96.5% to 97.5% for *FF* for MRF-Optim1 and to over 98% with MRF-Optim2, and from 93% to around 95% for $T1_{H2O}$). For both *FF* and $T1_{H2O}$ maps and both datasets, SSIM for MRF-Optim1 and MRF-Optim2 was significantly higher than for MRF T1-FF ($p < 0.05$). The sequences that performed the worst were MRF-Cohen and MRF-CRLB.

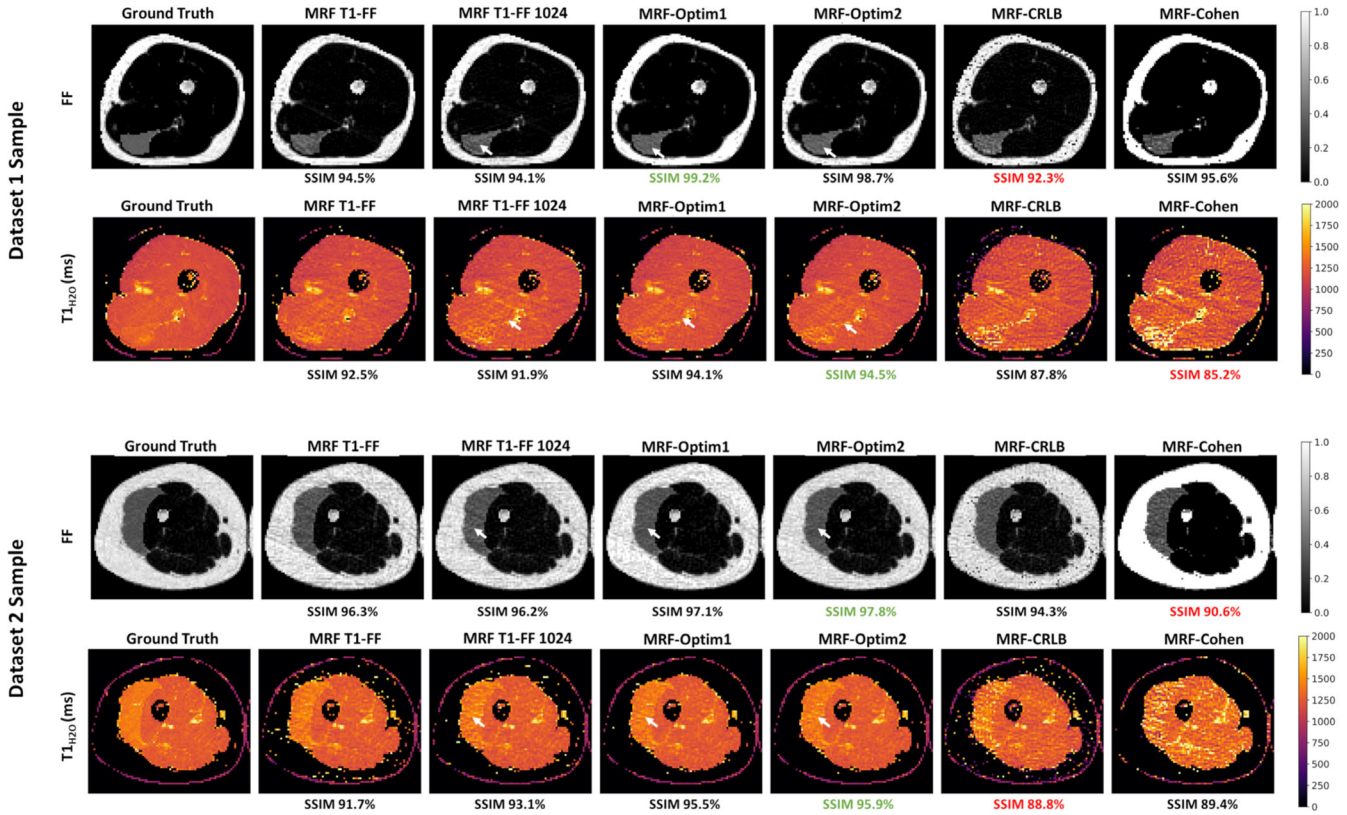

FIGURE 4 Sample $T1_{H20}$ and *FF* maps for the left thigh of one sample of Dataset 1 and the right thigh of one sample in Dataset 2 for all methods, with the ground truth shown in the left column. The white arrows show regions where streaking artifacts and noise are reduced with the sequences optimized with the proposed framework, with a zoomed-in image shown for MRF T1-FF 1 024, MRF-Optim1, and MRF-Optim2 in the white rectangle. SSIM for each method with the ground truth maps are shown, with the highest value highlighted in green and the lowest value highlighted in red.

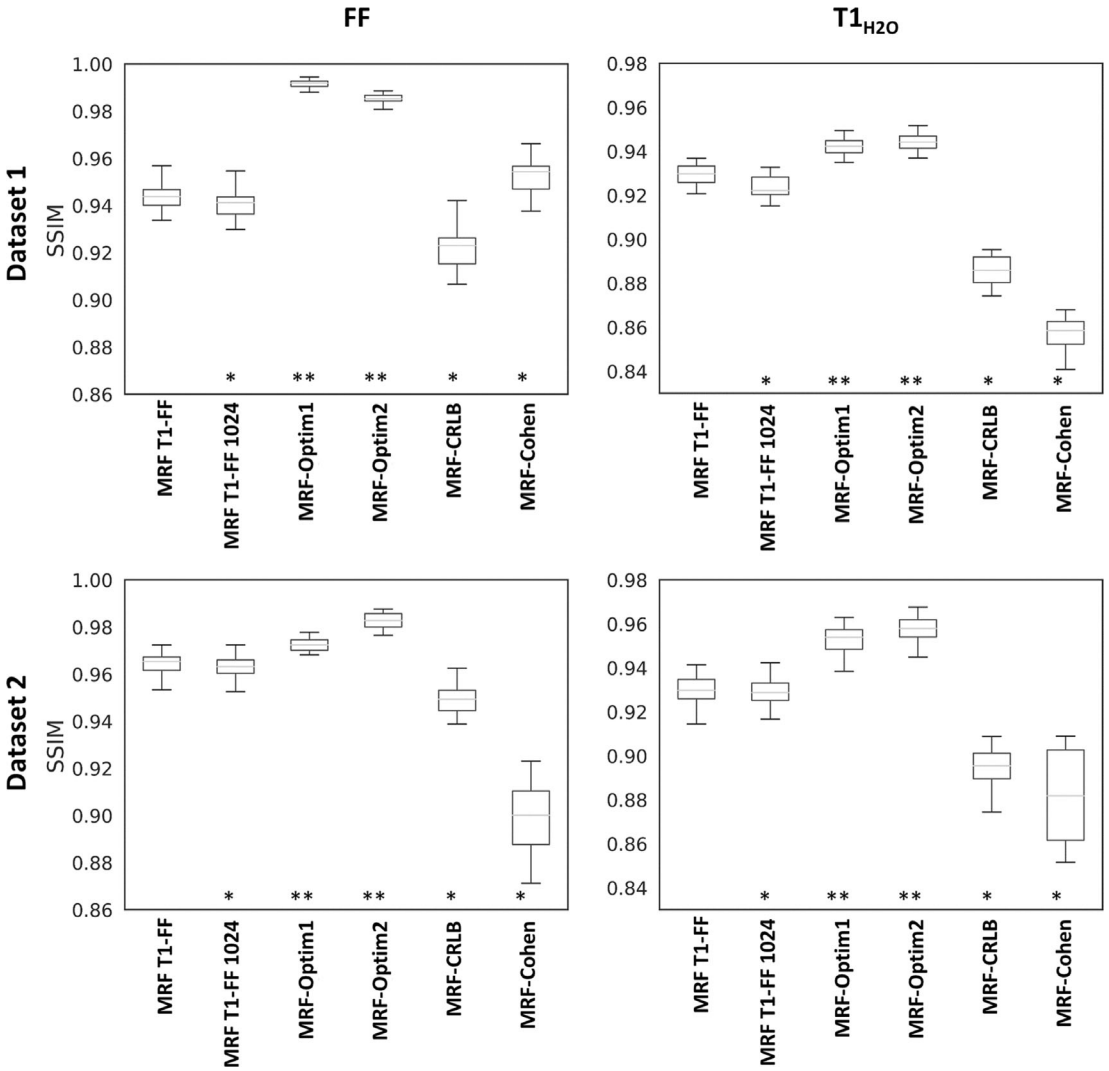

FIGURE 5 Boxplot showing the distribution of SSIM between the $T1_{H2O}$ and *FF* obtained with each sequence and the ground truth. A one-sided T-test with Bonferroni correction was calculated to test if the SSIM mean was less than the one of the original sequence: (*) p-value ≥ 0.05; (**) p-value < 0.05.

MRF-MRF-Optim2, which was optimized for both varying geometry and varying tissue parameters, appears to perform slightly better than MRF-Optim1 on Dataset 2, which contains more variability.

Bland-Altman plots of $T1_{H2O}$ and *FF* ROI-level errors against ground truth for all sequences across both datasets are shown in Figures 6 and 7, Figures S4 and S5. In both datasets, MRF T1-FF, MRF T1-FF 1 024, and MRF-CRLB overestimated low *FF* and underestimated high *FF*, resulting in an overall positive bias of approximately 0.01. MRF-Cohen *FF* values strongly underestimated low *FF* and overestimated high *FF*, consistent with the binary-like parametric maps described above. MRF-Optim1 and MRF-Optim2 exhibited no bias pattern across the whole *FF* range. For $T1_{H2O}$, MRF-Cohen was the only sequence showing a systematic overestimation of approximately 20 ms. In Dataset 1, MRF-Optim1 and MRF-Optim2 demonstrated higher precision than both MRF T1-FF 1 024 and MRF T1-FF (95% limits of agreement of 0.012 compared to more than 0.03 for *FF*, and 40 ms compared to 52 ms for MRF T1-FF and 66 ms for MRF T1-FF 1 024). In Dataset 2, 95% limits of agreement for *FF* improved from 0.05 for MRF T1-FF and more than 0.06 for MRF T1-FF 1 024 to less than 0.045 for MRF-Optim1 and MRF-Optim2. The 95% limits of agreement for $T1_{H2O}$ decreased from 53 ms for MRF T1-FF and more than 62 ms for MRF T1-FF 1 024 to 43 ms for MRF-Optim1 and 39 ms for MRF-Optim2. MRF-CRLB and MRF-Cohen were the least precise, with limits of agreement exceeding 100 ms and 200 ms, respectively. For *df*, MRF T1-FF, MRF T1-FF 1 024, MRF-Optim1, and MRF-Optim2 showed similar precision, with a confidence interval of around 5

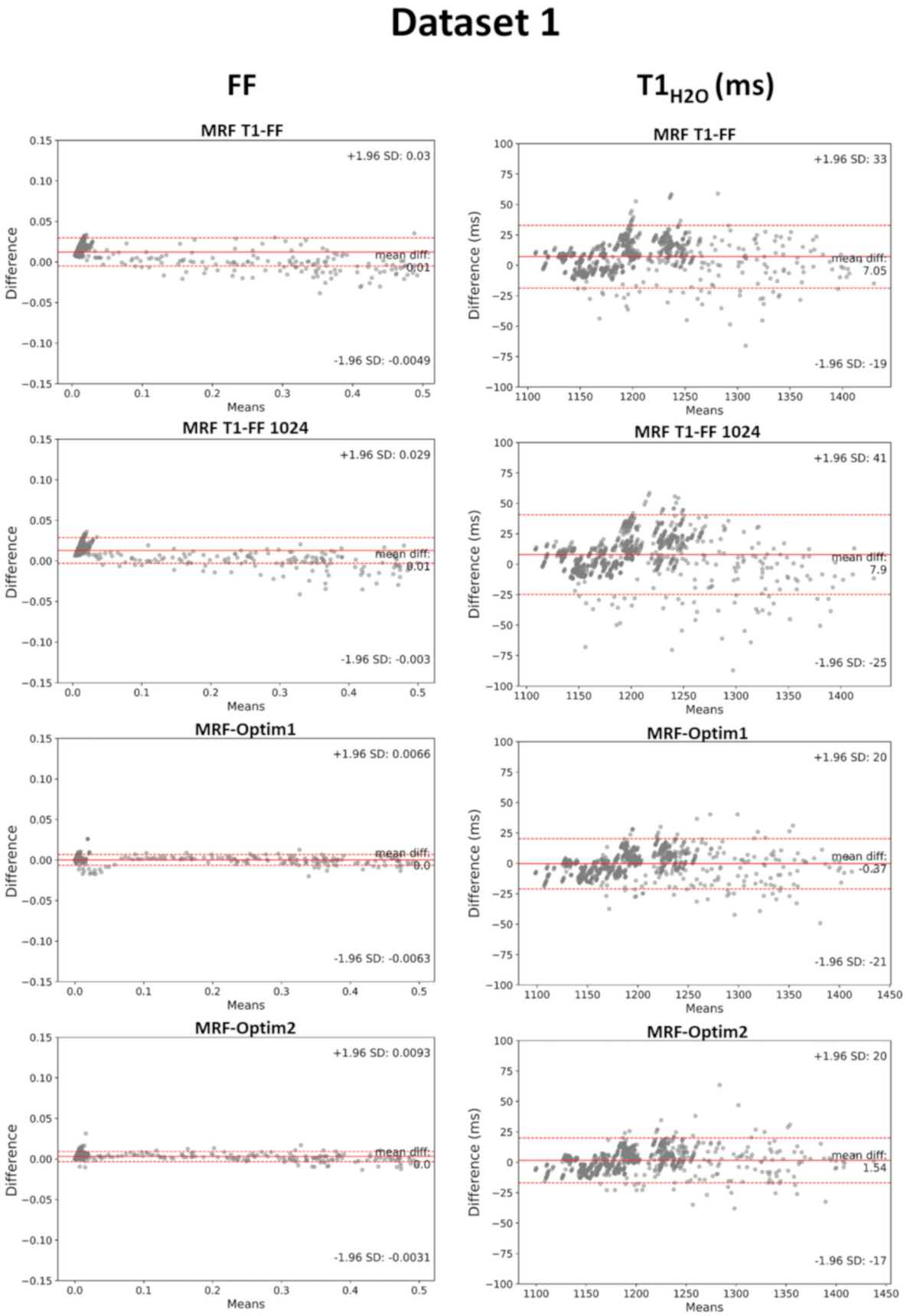

FIGURE 6 Bland-Altman plots showing the ROI-level errors against ground truth on *FF* and $T1_{H2O}$ for MRF T1-FF sequences and sequences optimized with the proposed framework, for dataset 1. Each point corresponds to an ROI in one of the samples. The plain red line is the mean error, the dashed red lines show the 95% confidence interval.

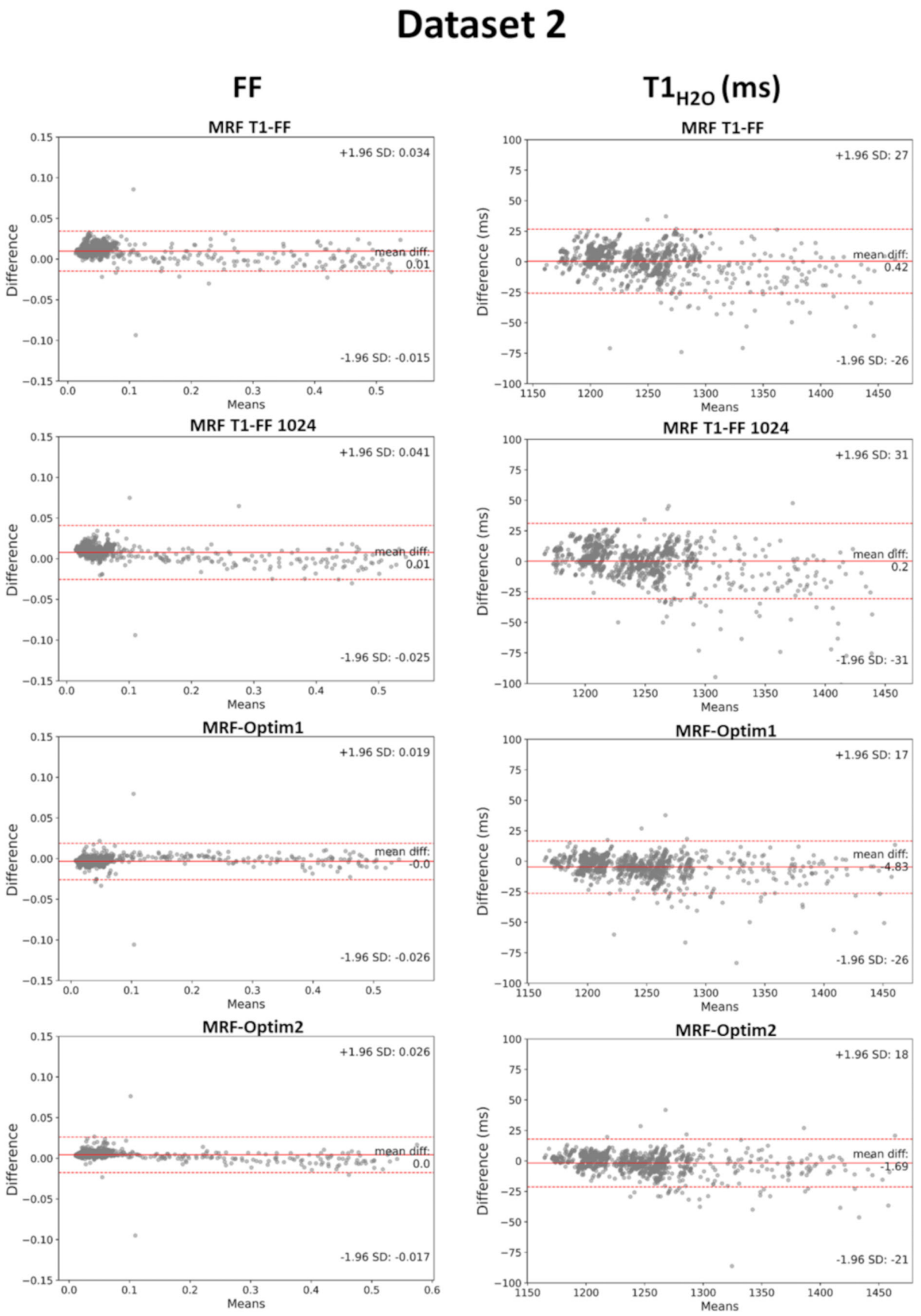

FIGURE 7 Bland-Altman plots showing the ROI-level errors against ground truth on *FF* and $T1_{H2O}$ for MRF T1-FF sequences and sequences optimized with the proposed framework, for dataset 2. Each point corresponds to an ROI in one of the samples. The plain red line is the mean error, the dashed red lines show the 95% confidence interval.

Hz for Dataset 2, while MRF-CRLB and MRF-Cohen decreased the precision to around 9 Hz for MRF-CRLB and 13 Hz for MRF-Cohen (Figures S6 and S7). For B1, MRF-Optim1 and MRF-Optim2 displayed similar limits of agreement to MRF T1-FF (around 0.05), whereas precision was degraded for MRF T1-FF 1 024, with limits of agreement of 0.07. MRF-CRLB and MRF-Cohen were again the least precise. No significant bias was observed for these parameters.

3.3 | In vivo validation

For in vivo maps, MRF-Optim1 and MRF-Optim2 effectively reduced the streaking artifacts and noise amplified by MRF T1-FF 1 024 (Figure 8), particularly evident in the $T1_{H2O}$ maps for SAR, GRA, SM and VL muscles. Quantitative maps computed from the MRF-Cohen sequence exhibited the poorest quality, similar to numerical phantoms results, with high noise, overestimation of $T1_{H2O}$, and *FF* values projected almost uniformly at 0 or 1. MRF-CRLB *FF* maps were blurry, and $T1_{H2O}$ maps showed pronounced streaking artifacts and noise, especially in the subject exhibiting a thicker subcutaneous fat layer (Subject 1). Corresponding *df* and B1 maps for the same subjects are shown in Supplementary Figure S8.

For *FF* estimation, the standard deviation per ROI increased for both MRF T1-FF 1 024 and MRF-CRLB compared to MRF T1-FF (Figure 9). In contrast, MRF-Optim1 and MRF-Optim2 improved precision relative to both MRF T1-FF 1 024 and MRF T1-FF. Consistent with the binary-like projection observed on *FF* maps, MRF-Cohen falsely appeared to be the most precise sequence for this parameter. Regarding $T1_{H20}$ maps, MRF-Optim1 and MRF-Optim2 exhibited precision comparable to MRF T1-FF, whereas MRF T1-FF 1 024 degraded it. The muscles with the highest parameter estimation variability for MRF T1-FF 1 024 were RF, SAR, and GRA. MRF-CRLB and MRF-Cohen displayed the highest standard deviations, confirming observations from the maps shown in Figure 8. All sequences, except MRF-Optim1 and MRF-Optim2, had a significant difference in mean standard deviation across all ROIs and patients compared to MRF T1-FF. As illustrated in Supplementary Figure S9, MRF T1-FF, MRF-Optim1, and MRF-Optim2 sequences displayed similar levels of standard deviation per ROI in *df* and B1

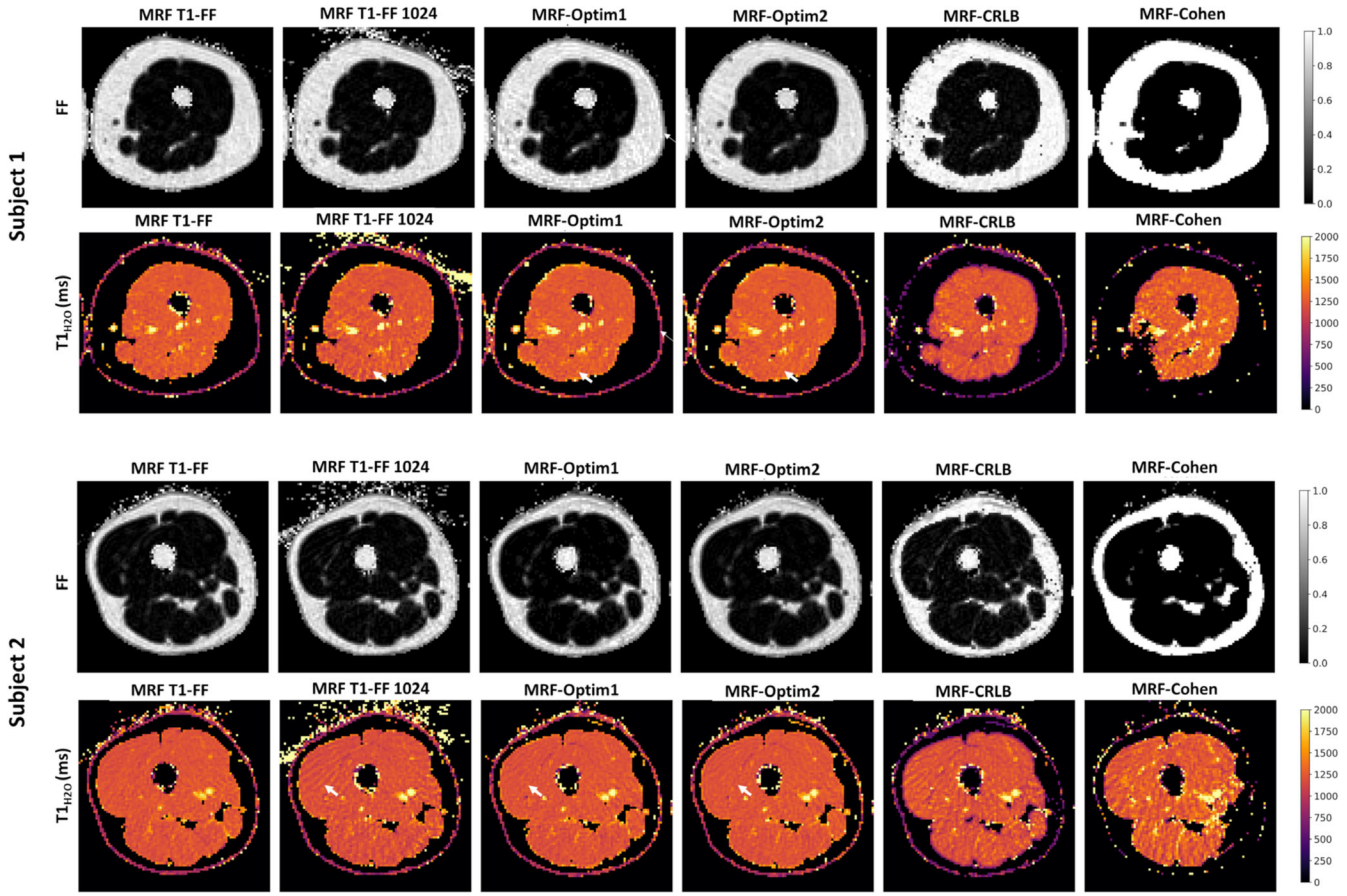

FIGURE 8 $T1_{H20}$ and *FF* maps for two in vivo acquisitions, displaying the left thigh for Subject 1 and the right thigh for Subject 2. The white arrows show regions where streaking artifacts and noise are reduced with the sequences optimized with the proposed framework.

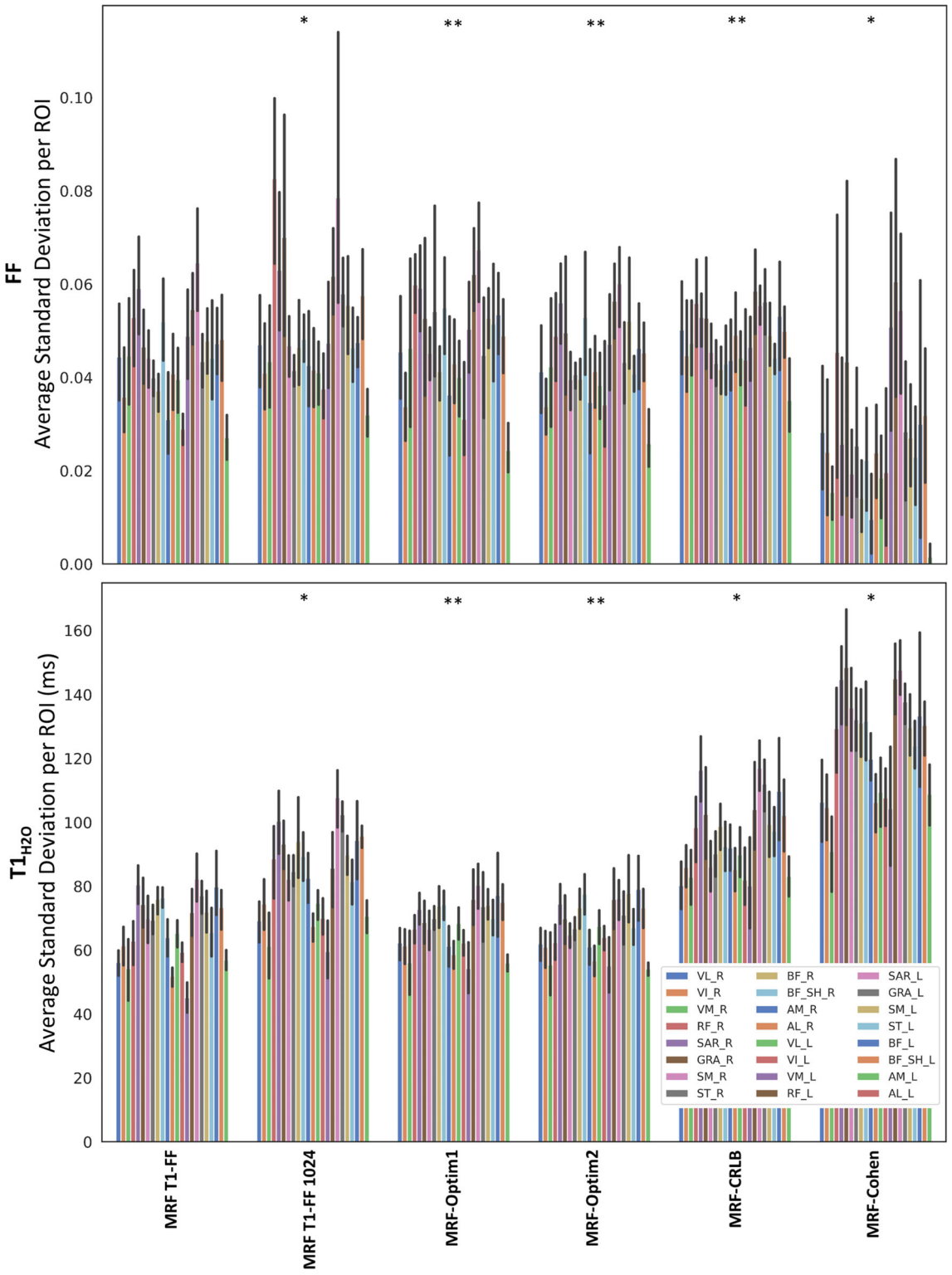

FIGURE 9 Barplot showing the average standard deviation for each ROI across all subjects for $T1_{H2O}$ and *FF*. The black bar indicates the 95% confidence interval. ANOVA test with Bonferroni correction was performed to check if the average standard deviation was equal between each sequence and MRF T1-FF: **p*-value < 0.05; ***p*-value ≥ 0.05.

parametric maps. The 3D in vivo acquisition with a higher in-plane resolution of 1 mm also showed a marked reduction in streaking artifacts, both in the axial and sagittal view, as illustrated in Figures S10 and S11.

4 | DISCUSSION

This study introduces a framework designed to accelerate MRF sequences while optimizing the accuracy and precision of parameter estimation. This framework was successfully applied to optimize a FLASH-based MRF sequence for quantitative muscle imaging, specifically targeting the measurement of FF and $T1_{H2O}$, while considering df, $B1$ and $T1_{Fat}$ confounding factors. We validated the framework on both realistic numerical thigh phantoms and in vivo in the thighs of ten healthy volunteers. The sequences optimized with the proposed framework reduced the original scan duration by approximately 30%, while improving the accuracy and precision of FF and $T1_{H2O}$ measures.

We compared our approach to optimization frameworks that consider the main source of noise as Gaussian such as those proposed by Cohen et al.[7] and Zhao et al.[9] The sequences that were optimized through these frameworks (MRF-Cohen and MRF-CRLB, respectively), revealed a systematic degradation in both accuracy and precision, with high-streaking artifacts and strong bias observed both in vivo and in numerical phantoms. The MRF-Cohen approach, despite decorrelating dictionary signals, performed the worst, exhibiting strong bias against ground truth $T1_{H2O}$ and FF and noise in all computed maps, particularly when the imaged thighs were characterized with a thicker layer of subcutaneous fat. This aligns with recent studies on MRF sequence optimization, which indicate that undersampling artifacts are the primary source of error in MRF, suggesting that other cost metrics may be inadequate for this particular application.[10,13] Therefore, an optimal MRF sequence optimization framework should consider the specific undersampling scheme to ensure incoherence between the variation of sequence parameters and the undersampling pattern.

Undersampling artifacts are object-dependent, so optimization frameworks considering undersampling might be prone to overfitting to the object shape or to the distribution of the parameters if a unique numerical phantom is used during the optimization process. In our framework, we mitigated this by creating a numerical phantom database with varying geometries and parameter distribution, from which the optimization framework randomly sampled during iterations. Slight overfitting was observed, as the performance of both MRF-Optim1 and MRF-Optim2 sequences was better on Dataset 1, which used a set of numerical phantoms with similar shapes as those used during optimization. However the performance of MRF-Optim1 and MRF-Optim2 on Dataset 2 and in vivo acquisitions was still better than the other optimized sequences. The B1 maps seemed to retain most of the streaking artefacts, without adverse impact on FF and $T1_{H2O}$. The MRF-Optim2 sequence, which was optimized on a richer numerical phantom database including geometrical and tissue parameter variation, generalized better, being more accurate on Dataset 2, and showing slightly improved precision in vivo. Overfitting to a specific phantom shape may present less of an issue in the brain, where geometric variability between subjects is relatively minor, compared to other applications like muscle, liver, and heart. For whole-body protocols, one would have to make a choice between optimizing a single sequence using a large database that includes the diverse shapes and parameters of different body parts, or optimizing a separate sequence for each region. The latter approach could offer more precise estimations, but it might introduce biases between regions due to the use of different sequences.

The recovery time at the end of each repetition of the MRF scheme was reduced, using an efficient calculation with an analytical equation and including it as an optimized parameter in the framework. The recovery time never reached zero, likely because maintaining sufficient SNR for encoding parameters was necessary. To reduce the optimization problem dimensionality, the TE schedule was kept similar in shape (three constant TE steps) to the original MRF T1-FF sequence, and the FA schedule was parameterized by a small number of variables. However, the FA schedules of MRF-Optim1 and MRF-Optim2 converged to a simple single-peak curve, lying in a lower dimension space than the one spanned by the parameterization. The optimization framework was implemented for FLASH-like sequences, but could be extended to FISP and TrueFISP MRF sequences by calculating the associated steady-state initial longitudinal magnetization M_z^{SS}. More broadly, the optimization framework was limited to spoiled MRF sequences with initial inversion and variable flip angles for T1 mapping, as well as variable echo times for FF mapping. Sequences acquiring data with multiple inversion times in place of variable flip angles, which are less sensitive to B1 variations but result in longer scan times,[31] were not considered in the optimization process. Rather than minimizing estimation errors in B1 maps, an alternative approach would be to design a sequence that is intrinsically less sensitive to this confounding factor, a strategy that has proven effective for $T1_{H2O}$ mapping.[32] This could be achieved by imposing a lower bound on the nominal FA.

In skeletal muscle applications, intramuscular FF is commonly derived from multi-echo GRE sequences combined with Dixon-like reconstruction approaches.[33] The original MRF T1-FF sequence has demonstrated high-precision and accuracy in FF estimation when compared with Dixon methods, both in phantoms and in subjects with neuromuscular diseases.[4,5] Additionally, $T1_{H2O}$ measurements from the MRF T1-FF sequence have been validated against reference spectroscopic approaches in both phantoms and in vivo.[4] Given this extensive validation, the original MRF T1-FF sequence served as a reference for evaluating the optimized sequences in the present study.

Active muscle damage is typically assessed non-specifically using $T2_{H2O}$ quantification from 2D multi-spin echo acquisitions.[34] Recent studies have highlighted strong correlations between $T1_{H2O}$ and $T2_{H2O}$ across various muscle conditions, including inflammatory myopathies[5] facioscapulohumeral dystrophy,[35] and aging.[36] Unlike MSE sequences, the MRF T1-FF acquisition is not constrained by specific absorption rate limitations and is inherently compatible with 3D imaging in shorter acquisition times than MSE.[21] However, simultaneously estimating $T1_{H2O}$ and $T2_{H2O}$ could provide additional insight into neuromuscular disease mechanisms. The proposed framework could be extended to non-spoiled fast GRE sequences sensitive to both relaxation processes.

An other limitation of this study is that the sequences were not tested on a large cohort of subjects with neuromuscular diseases. This was mitigated by validation on numerical Datasets 1 and 2, which generated phantoms by varying FF and $T1_{H2O}$ in arbitrarily chosen regions of interest, mimicking alterations generally observed in subjects with neuromuscular diseases. Future work should confirm these findings with in vivo data. Additionally, due to heavy computing requirements and optimization time, the framework was performed on 2D numerical phantoms, but was tested on 3D in vivo acquisitions, as 3D is more relevant for sequence acceleration. Although precision improvements compared to a shortened version of MRF T1-FF were observed, ideally, 3D undersampling patterns should be tested in optimization simulations to further accelerate acquisitions. Evaluating the ability of the optimized sequences to generalize across different anatomical regions and spatial resolutions, such as isotropic acquisitions, would be an interesting direction for future research. Moreover, while this study used a direct nuFFT transformation, several MRF reconstruction frameworks use iterative low-rank reconstructions to mitigate residual undersampling artifacts. Including these iterative reconstruction approaches in the framework could further enhance optimization but was not feasible due to the high-computational burden.

5 | CONCLUSION

In conclusion, we introduced an MRF sequence optimization framework that accounts for the steady state reached after a few repetitions by shortening the recovery time of the GRE-based echo train using an analytical formula. This framework also simulates undersampling artifacts on a database of realistic numerical thigh phantoms with varying shapes and tissue parameter distribution to mitigate overfitting. We applied it to optimize the MRF T1-FF sequence, previously introduced to estimate $T1_{H2O}$, $T1_{Fat}$, FF, off-resonance frequency df, and B1 in skeletal muscle applications. Our framework produced two sequences that significantly improved the accuracy and precision of the estimated parameters in both numerical simulations and in vivo, with a visual reduction of noise and streaking artifacts in parametric maps. Sequences optimized by minimizing the correlation between dictionary signals or Cramer-Rao lower bound underperformed, showing significant bias and artifacts in the corresponding parametric maps. This framework paves the way for fast 3D quantitative imaging in the skeletal muscle with several potential applications in the field of neuromuscular disorders.

FUNDING INFORMATION

This work was supported by the French National Research Agency (ANR-20-CE19-0004) and the Association Institut de Myologie.

CONFLICT OF INTEREST STATEMENT

The authors declare no potential conflict of interest.

DATA AVAILABILITY STATEMENT

De-identified data used during the study and supporting code are available from the corresponding author upon request.

ORCID

Constantin Slioussarenko https://orcid.org/0009-0009-5822-6911

Benjamin Marty https://orcid.org/0000-0002-4983-647X

REFERENCES

1. Ma D, Gulani V, Seiberlich N, et al. Magnetic resonance fingerprinting. *Nature*. 2013;495:187-192.

2. Jaubert O, Cruz G, Bustin A, et al. Water-fat Dixon cardiac magnetic resonance fingerprinting. *Magn Reson Med*. 2020;83:2107-2123.
3. Velasco C, Cruz G, Jaubert O, Lavin B, Botnar RM, Prieto C. Simultaneous comprehensive liver T1, T2, T2*, T1ρ, and fat fraction characterization with MR fingerprinting. *Magn Reson Med*. 2022;87:1980-1991.
4. Marty B, Carlier PG. MR fingerprinting for water T1 and fat fraction quantification in fat infiltrated skeletal muscles. *Magn Reson Med*. 2020;83:621-634.
5. Marty B, Reyngoudt H, Boisserie J-M, et al. Water-fat separation in MR fingerprinting for quantitative monitoring of the skeletal muscle in neuromuscular disorders. *Radiology*. 2021;300:652-660.
6. Marty B, Baudin P-Y, d Araujo ECA, Fromes Y, Wahbi K, Reyngoudt H. Assessment of extracellular volume fraction in Becker muscular dystrophy by using MR fingerprinting. *Radiology*. 2023;307:221115.
7. Cohen O, Rosen MS. Algorithm comparison for schedule optimization in MR fingerprinting. *Magn Reson Imaging*. 2017;41:15-21.
8. Sommer K, Amthor T, Doneva M, Koken P, Meineke J, Börnert P. Towards predicting the encoding capability of MR fingerprinting sequences. *Magn Reson Imaging*. 2017;41: 7-14.
9. Zhao B, Haldar JP, Liao C, et al. Optimal experiment design for magnetic resonance fingerprinting: Cramér-rao bound meets spin dynamics. *IEEE Trans Med Imaging*. 2019;38: 844-861.
10. Jordan SP, Hu S, Rozada I, et al. Automated Design of Pulse Sequences for magnetic resonance fingerprinting using physics-inspired optimization. *Proc Natl Acad Sci USA*. 2021;118:e2020516118.
11. Hu S, Jordan S, Boyacioglu R, et al. A fast MR fingerprinting simulator for direct error estimation and sequence optimization. *Magn Reson Imaging*. 2023;98:105-114.
12. Stolk CC, Sbrizzi A. Understanding the combined effect of *k* -space Undersampling and transient states excitation in MR fingerprinting reconstructions. *IEEE Trans Med Imaging*. 2019;38:2445-2455.
13. Heesterbeek DG, Koolstra K, van Osch MJ, van Gijzen MB, Vos FM, Nagtegaal MA. Mitigating Undersampling errors in MR fingerprinting by sequence optimization. *Magn Reson Med*. 2023;89:2076-2087.
14. Kraft D. A software package for sequential quadratic programming. *Forschungsbericht- Deutsche Forschungs- und Versuchsanstalt fur Luft- und Raumfahrt*. Wiss. Berichtswesen d. DFVLR; 1988.
15. Zur Y, Stokar S, Bendel P. An analysis of fast imaging sequences with steady-state transverse magnetization refocusing. *Magn Reson Med*. 1988;6:175-193.
16. Chavhan GB, Babyn PS, Jankharia BG, Cheng H-LM, Shroff MM. Steady-state MR imaging sequences: physics, classification, and clinical applications. *Radiographics*. 2008;28: 1147-1160.
17. Zur Y, Wood ML, Neuringer LJ. Spoiling of transverse magnetization in steady-state sequences. *Magn Reson Med*. 1991;21:251-263.
18. Cloos MA, Knoll F, Zhao T, et al. Multiparametric imaging with heterogeneous radiofrequency fields. *Nat Commun*. 2016;7:12445.
19. Koolstra K, Webb AG, Veeger TTJ, Kan HE, Koken P, Börnert P. Water–fat separation in spiral magnetic resonance fingerprinting for high temporal resolution tissue relaxation time quantification in muscle. *Magn Reson Med*. 2020;84:646-662.
20. Amthor T, Doneva M, Koken P, Sommer K, Meineke J, Börnert P. Magnetic resonance fingerprinting with short relaxation intervals. *Magn Reson Imaging*. 2017;41:22-28.
21. Marty B, Lopez Kolkovsky AL, Caldas de Almeida Araújo E, Reyngoudt H Quantitative skeletal muscle imaging using 3D MR fingerprinting with water and fat separation. *J Magn Reson Imaging*. 2021;53:1529-1538.
22. Barnett AH. Aliasing error of the exp() kernel in the nonuniform fast Fourier transform. *Appl Comput Harmon Anal*. 2021;51:1-16.
23. Barnett AH, Magland JF, Klinteberg L A parallel non-uniform fast Fourier transform library based on an "exponential of semicircle". *Kernel*. 2018;41:C479-C504.
24. Slioussarenko C, Baudin P-Y, Reyngoudt H, Marty B. Bi-component dictionary matching for MR fingerprinting for efficient quantification of fat fraction and water T1 in skeletal muscle. *Magn Reson Med*. 2024;91:mrm.29901.
25. Storn R, Price K. A simple and efficient heuristic for global optimization over continuous spaces. *J Glob Optim*. 1997;11:341-359.
26. Feng L. Golden-angle radial MRI: basics, advances, and applications. *J Magn Reson Imaging*. 2022;56:45-62.
27. Reyngoudt H, Smith FE, de Almeida Araújo EC, et al. Three-year quantitative magnetic resonance imaging and phosphorus magnetic resonance spectroscopy study in lower limb muscle in Dysferlinopathy. *J Cachexia Sarcopenia Muscle*. 2022;13: 1850-1863.
28. Reyngoudt H, Baudin P-Y, de Almeida Araújo EC, et al. Effect of Sirolimus on muscle in inclusion body myositis observed with magnetic resonance imaging and spectroscopy. *J Cachexia Sarcopenia Muscle*. 2024;15:1108-1120.
29. Azzabou N, Reyngoudt H, Carlier PG. Using a generic model or measuring the intramuscular lipid Spectrum: impact on the fat infiltration quantification in skeletal muscle. *Proc. 25th ISMRM*; 2017:A5189.
30. Wang Z, Bovik A, Sheikh H, Simoncelli E. Image quality assessment: from error visibility to structural similarity. *IEEE Trans Image Process*. 2004;13:600-612.
31. Verloh N, Fuhrmann I, Fellner C, et al. Quantitative analysis of liver function: 3D variable-Flip-angle versus look-locker T1 Relaxometry in hepatocyte-specific contrast-enhanced liver MRI. *Quant Imaging Med Surg*. 2022;12:2509-2522.
32. Huaroc Moquillaza E, Weiss K, Stelter J, et al. Accelerated liver water T1 mapping using single-shot continuous inversion-recovery spiral imaging. *NMR Biomed*. 2024;37:e5097.
33. Burakiewicz J, Sinclair CDJ, Fischer D, Walter GA, Kan HE, Hollingsworth KG. Quantifying fat replacement of muscle by quantitative MRI in muscular dystrophy. *J Neurol*. 2017;264:2053-2067.
34. Carlier PG, Marty B, Scheidegger O, et al. Skeletal muscle quantitative nuclear magnetic resonance imaging and spectroscopy

as an outcome measure for clinical trials. *J Neuromuscular Diseases*. 2016;3:1-28.
35. Gerhalter T, Marty B, Gast LV, et al. Quantitative 1H and 23Na muscle MRI in Facioscapulohumeral muscular dystrophy patients. *J Neurol*. 2021;268:1076-1087.
36. Lopez Kolkovsky AL, Matot B, Baudin P-Y, et al. Multiparametric aging study across adulthood in the leg through quantitative MR imaging, ^{1}H spectroscopy, and ^{31}P spectroscopy at 3T. *Magn Reson Imaging*. 2025;61:347-361.

SUPPORTING INFORMATION

Additional supporting information may be found in the online version of the article at the publisher's website.

Data S1. Supporting Information.

How to cite this article: Slioussarenko C, Baudin P-Y, Marty B. A steady-state MR fingerprinting sequence optimization framework applied to the fast 3D quantification of fat fraction and water T1 in the thigh muscles. *Magn Reson Med*. 2025;93:2623-2639. doi: 10.1002/mrm.30490